Natural Resources Research, Vol. 28, No. 3, July 2019 (© 2018)
https://doi.org/10.1007/s11053-018-9445-9

Original Paper

Discriminating Weathering Degree by Integrating Optical Sensor and SAR Satellite Images for Potential Mapping of Groundwater Resources in Basement Aquifers of Semiarid Regions

Luís André Magaia,[1,2] Katsuaki Koike,[1,4] Tada-nori Goto,[1] and Alaa Ahmed Masoud[3]

Received 18 August 2018; accepted 11 December 2018
Published online: 19 December 2018

Unlike in coastal and sedimentary basins, regional-scale exploration of groundwater resources using only geophysical methods is costlier in consolidated rocks such as volcanic rocks and crystalline basement complexes in Africa because of the highly heterogeneous structure of aquifers. Therefore, advanced analysis of remotely sensed images and an accurate assessment of groundwater resources are crucial before carrying out a geophysical prospecting survey. This study proposed a joint analysis of satellite images from optical sensors and synthetic aperture radar (SAR) which aimed to enhance potential mapping accuracy of groundwater resources in crystalline rock areas in a semiarid region. The backscattering coefficient of the SAR data analysis effectively detected the zones of relatively high weathering degree and thus having thick permeable regolith. In addition, a modified clay index calculated from the four band reflectances of the optical sensor image—red, near infrared, and two shortwave infrared bands—was applied to discriminate clay-rich zones from high vegetation activity zones. The clay-rich zones detected corresponded with the highly weathered zones estimated from the small SAR backscattering coefficients. The zones also corresponded with a large density of faults and lineaments and furthermore were verified by high potential yields from groundwater wells. The thickness of weathered zones was likely to increase with a decreasing backscattering coefficient and higher modified clay index values. Conversely, large backscattering coefficients in the narrow zones along the major lineaments from large volumetric scattering because of high vegetation activity, as confirmed by the large vegetation index values, suggested that high moisture content was retained in the soils. In fact, the potential yields of the groundwater wells tended to increase near the lineaments. Accordingly, shallow groundwater occurrence is plausible in those zones.

KEY WORDS: Regolith, Backscattering coefficient, Vegetation index, Clay index, Lineament, Mozambique.

INTRODUCTION

Groundwater is a crucial water source for industry, agriculture, and daily life across the world, particularly in Africa which has extensive arid and semiarid regions. Groundwater occurrence in such

[1]Department of Urban Management, Graduate School of Engineering, Kyoto University, Kyoto 615-8540, Japan.
[2]Geology Department, Faculty of Sciences, Eduardo Mondlane University, Ave. Mozambique km 1.5, P.O. Box 257, Maputo, Mozambique.
[3]Geology Department, Faculty of Science, Tanta University, Tanta 31527, Egypt.
[4]To whom correspondence should be addressed; e-mail: koike.katsuaki.5x@kyoto-u.ac.jp

1520-7439/19/0700-1197/0

regions, especially those with hard rocks, is scarce because of low precipitation and high evapotranspiration rates (Wright 1992). The occurrence and flows of groundwater are mainly controlled by the distribution and properties of mechanically weak zones of rocks that have been affected by fracturing, faulting, and weathering (Wright 1992; National Research Council 1996; Foster 2012). Such zones are capable of storing and transmitting more groundwater than intact rocks. A close relationship between water yields at wells and the thickness of the weathered zone in crystalline rocks has been reported in many areas (e.g., Jones 1985; Wright 1992; Chirindja et al. 2017) where groundwater serves as the main factor of weathering that forms regolith aquifers through hydrolysis and dissolution. In addition to fracturing and faulting, weathering is controlled by several other factors including rock texture, porosity, and crack density, but the duration of basement rock exposure to the atmosphere is the most important (Jones 1985; Acworth 1987; Worthington et al. 2016; Rocchi et al. 2017).

Mapping the extent and thickness of weathered zones in a target area requires a sufficient number of drilled wells and regional geophysical surveys, of which electric sounding and electromagnetic surveys are the most common. Owing to the strong heterogeneities of basement aquifers generated from crystalline rocks, many geophysical surveys with dense intervals are necessary, but the costs of these are not generally practical in African countries. However, satellite remote sensing using optical and radar images combined with well data is cheaper.

Optical images of reflectance spectral data provide useful information on physiological activity of vegetation and distribution of specific soil or rock type. This feature can contribute to potential mapping of groundwater in crystalline basements (Shaban et al. 2006; Petrakis et al. 2016; Magaia et al. 2018). A major advantage of the radar system over the optical sensor system is that it can acquire imagery day or night regardless of weather conditions and cloud cover (Engman 1991). This advantage has been used in semiarid regions of Africa for groundwater resource assessment by hydrogeological mapping and lineament extraction (e.g., Koch and Mather 1997; Corgne et al. 2010). The backscattering energy of synthetic aperture radar (SAR) imagery is directly related to soil moisture in addition to surface roughness (Engman 1991; Shi et al. 1997; Gharechelou et al. 2015; Saepuloh et al. 2015); thus, it can be used for detecting recharge and discharge zones. In addition, the backscattering is affected by vegetation cover (Trudel et al. 2012; Kornelsen and Coulibaly 2013; Sabaghy et al. 2018). To avoid such affect, the use of SAR imagery would be more beneficial for arid and semiarid regions with sparse vegetation cover.

As weathering progresses, water–rock interaction decomposes and dissolves rocks and, consequently, produces secondary minerals. Physical and mechanical properties are also degraded, accentuating erosion rate and increasing surface roughness in slope areas, while smoothing the surface in low gradient areas through the formation of clay minerals (Jones 1985; Rocchi et al. 2017). Specular reflection of the incident microwave energy is predominant in such flat areas where regolith aquifers tend to be formed on top of the fractured bedrock. Here, regolith is defined as weathered and transported materials overlying intact bedrock (Jones 1985; Wilford et al. 2016).

Based on the foregoing background, our research aimed to use both optical sensor and SAR imagery data for increasing potential mapping accuracy for groundwater resources in crystalline basement rock and regolith areas in arid and semiarid regions. The surface backscattering coefficients of SAR data from two microwave frequencies were combined with vegetation and clay indices derived from optical sensor, Sentinel-2 imagery, to assess the weathering degree of crystalline basement rocks. The proposed method is intended to discriminate highly weathered zones in an efficient and cost-effective manner and enhance the success rate of drilling to locate aquifers in areas without detailed groundwater information. To the best of our knowledge, this is the first study that successfully combines optical sensor and SAR imagery data for discriminating weathering degree and groundwater potential mapping in basement aquifers of semiarid regions.

GEOLOGICAL AND HYDROGEOLOGICAL SETTINGS

The study area is located in the northeast of Tete Province in central Mozambique, partially covering the Angonia and Tsangano districts in the west and south, respectively, from 14°27′50″S, 34°09′30″E to 14°53′00″S, 34°34′30″E. This area was selected because it is typical of African semiarid land surfaces and geology and needs more groundwater for irrigation and livestock farming. The study area is approximately 2000 km^2 and is characterized by smooth plateaus and mountains with elevations of 700–2000 m a.s.l. with some scattered inselbergs, long valleys, and plains (Fig. 1).

This area is overlain by rocks of the Mesoproterozoic and Neoproterozoic crystalline basement complex. They are classified into two main groups, the Ulongue Suite and Angonia Group (Fig. 2). The Ulongue Suite consists of younger plutons of the Dedza monzonite and related syenitic rocks, the Metengo-Balame anorthosite (hereinafter termed MBA), and the Tomo-Gimo mafic gneiss rocks. The older plutons of the Furancungo Suite, mainly the Desaranhama granites and related felsic rocks, partly cover the southwestern corner of the study area. The Angonia Group rocks are the oldest in the study area and are chiefly composed of volcanic and highly metamorphized rocks distributed discontinuously in a NW–SE direction. The Angonia Group rocks with the smallest extent are quartzite and marble units and those with the largest extent are biotite–hornblende–quartz–feldspar banded gneiss (hereinafter termed BBG) (CGS 2007).

The hydrogeology of the study area has been studied only by DNA (1987) and Magaia et al. (2018). A 1:1,000,000 scale hydrogeological map of Mozambique (DNA 1987) depicts wide or narrow distributions of aquifers ranked as limited productivity (< 5 m^3/h) with low-to-very-low permeability (C1) and areas of limited groundwater occurrence (< 3 m^3/h) with very low permeability (C2). One noted feature is the development of fractured aquifers in the MBA unit (B3), with moderate productivity (3–10 m^3/h) and low permeability. The mountainous zones are practically devoid of groundwater because of their very-low-to-zero permeability (C3) (DNA 1987).

The climate of the study area is dry and tropical, and most of the precipitation falls in the period between December and March. Based on meteorological station data from the Meteorology Institute of Mozambique (INAM) in the Ulongue village in the middle of the study area, the mean annual precipitation between 1965 and 1984 was 905 mm. Mozambique has experienced long periods of drought, which have caused serious damage to agriculture and cattle farming and shortages of drinking water across the country.

MATERIALS AND METHODS

Satellite Imagery and Preprocessing

For accurate estimation of weathering degree, two microwave frequencies and dual polarization of SAR data were used: one scene of Phased Array type L band Synthetic Aperture Radar (PALSAR) data onboard the Advanced Land Observing Satellite (ALOS) launched in 2006 (Rosenqvist et al. 2007) and two scenes of C band data from Sentinel-1A launched in 2014. The wavelength of L band (23.6 cm) is longer than that of C band (5.6 cm). The specifications of these SAR data are summarized in Table 1. The spatiotemporal variability in the features suggesting richness of groundwater and shallowness of water level, such as soil moisture and vegetation activity, was expected to be clarified by the differences in the band and season of acquisition date (dry or rainy) of the SAR data.

The selected PALSAR data supplied by the Alaska Satellite Facility (ASF DAAC 2015) were fully multi-looking images processed for noise reduction. For the Sentinel data, multi-looking processing and calibration and radiometric correction were performed using the Sentinel's Application Platform (SNAP) toolbox (Laur et al. 2004), and geometric correction was adopted using the range Doppler geometric correction operator and the 3-arc second SRTM DEM data (Small and Schubert 2008).

As optical sensor imagery, one scene of Sentinel-2A level 1C, which was the best quality in the dry season, was selected to map vegetation cover and activity and to discriminate the development of clay minerals in the regolith. Details of scene data and specifications of the bands selected for our analysis in terms of wavelength and spatial resolution are summarized in Tables 2 and 3, respectively. Atmospheric, geometric, and cirrus corrections to transform the original top-of-atmosphere level 1C data to the bottom-of-atmosphere level 2A data were implemented using the Sen2Cor processor in the SNAP toolbox (Mueller-Wilm 2017) prior to the computation of spectral indices.

Surface Backscattering Coefficient

In the active radar system, surface properties are characterized indirectly through a parameter, surface backscattering coefficient. This parameter is

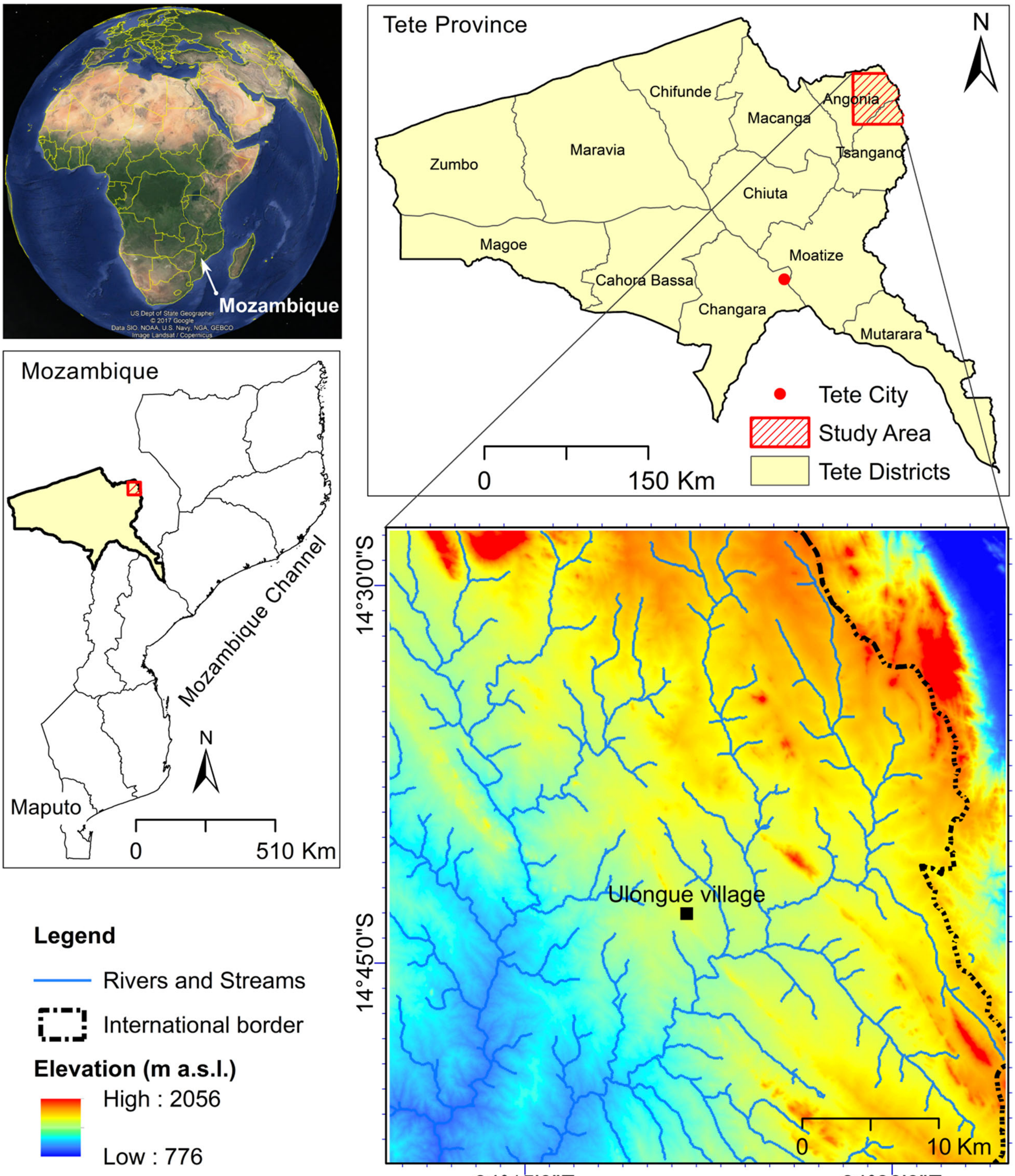

Figure 1. Location of the study area in the Tete Province, central western Mozambique, and its topography based on a gridded image of digital elevation model (DEM) from the Shuttle Radar Topographic Mission (SRTM). The eastern side of the study area is contiguous to Malawi as shown by the international border.

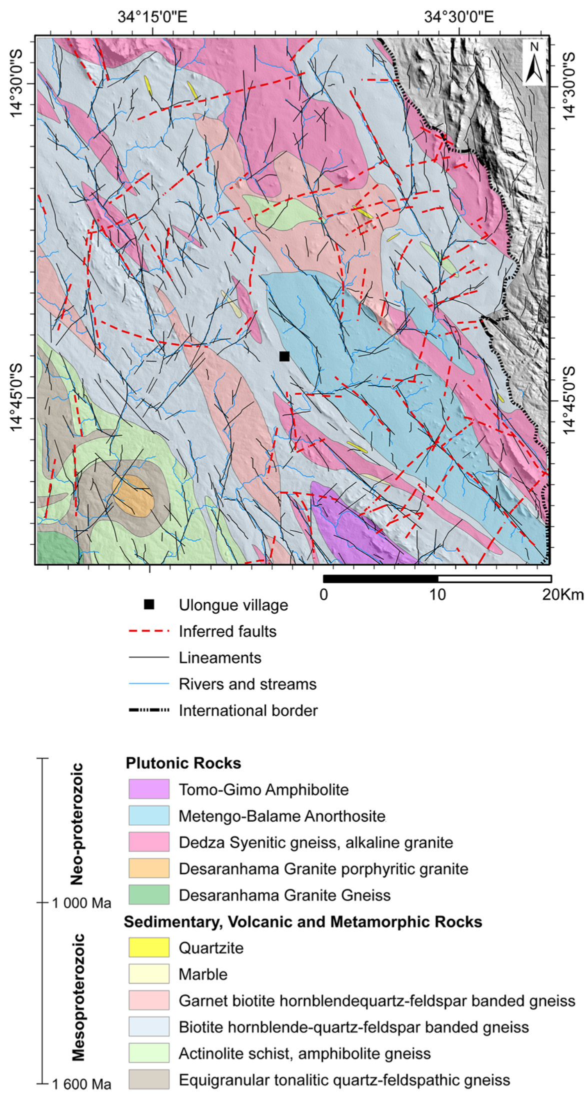

Figure 2. Simplified geological map of the study area digitized from the 1:250,000 scale map (DNG 2006). This map is overlaid on a shaded relief SRTM DEM and lineaments extracted from multi-shaded SRTM DEM data (Magaia et al. 2018).

calculated from the pixel value of SAR data as follows.

In a bi-static radar system, the backscattering power received by a radar antenna (P_r) from an area A of the scattering on the Earth's surface is defined as (Rees 2001):

$$P_r = \frac{\lambda^2 G^2 P_t}{(4\pi)^3 \eta R^4} \sigma^0 A \quad (1)$$

where λ is wavelength of the microwave, η is antenna efficiency, $G = 4\pi A / \lambda^2$ is antenna gain, P_t is transmitting power of the antenna, R is distance between the antenna and scattering target on the Earth's surface, and σ^0 is the dimensionless surface backscattering (dB). In general, σ^0 is a function of the roughness and dielectric permittivity of surface materials and varies with the incidence angle of the radar beam (Engman 1991; Rees 2001).

The original ALOS PALSAR image data at level-1.5 product are composed of a set of digital numbers of the microwave amplitude (DNs) that are 16-bit unsigned short integers. The DNs are converted into σ^0 by the following equation (Shimada et al. 2009):

$$\sigma^0 = 10 \cdot \log_{10}(\mathrm{DN})^2 + K \quad (2)$$

where K is calibration factor depending on the type of polarization and data acquisition period. Its value is $-$ 83.2 or $-$ 80.2 dB depending on the fine beam dual mode, HH or HV, respectively. The DNs of Sentinel-1A data can be converted to σ^0 by the equation of Miranda and Meadows (2015); thus,

$$\sigma^0 = 10 \cdot \log_{10}\left(\frac{\mathrm{DN}^2}{A_{\mathrm{dn}}^2 K} \cdot \sin\alpha\right), \quad (3)$$

Table 1. Specifications of Phased Array type L band Synthetic Aperture Radar (PALSAR) and Sentinel-1A data used in this study

Acquisition date	Season	Band	Wavelength (cm)	Pixel spacing (m)	Mode/ polarization	Off-nadir angle (°)	Satellite/orbit
July 5, 2007	Dry	L	23.6	12.5 × 12.5	FBD/HH and HV	34.3	ALOS/Ascending
January 3, 2015	Rainy	C	5.6	10 × 10	IW/VV and VH	26–40.4	Sentinel-1A/Descending
September 13, 2017	Dry	C	5.6	10 × 10	IW/VV and VH	26–40.4	Sentinel-1A/Descending

FBD and IW stand for fine beam dual and interferometric wide swath modes of acquisition, respectively

Table 2. Specification of Sentinel-2A scene data for analysis of vegetation and clay indices

Acquisition date	Season	Processing level	Sensing start time	Cloud cover	Orbit	Tile number	Relative orbit
September 26, 2017	Dry	Level-1C	07:36:41	0%	Descending	36LXJ	092

Table 3. Specification of Sentinel-2A spectral bands

Band number	Band name	Central wavelength (nm)	Bandwidth (nm)	Spatial resolution (m)
1	Coastal aerosol	443.9	27	60
2	*Blue*	*496.6*	*98*	*10*
3	*Green*	*560.0*	*45*	*10*
4	*Red*	*664.5*	*38*	*10*
5	Vegetation red edge 1	703.9	19	20
6	Vegetation red edge 2	740.2	18	20
7	Vegetation red edge 3	782.5	28	20
8	Near infrared	835.1	145	10
8A	*Narrow near infrared*	*864.8*	*33*	*20*
9	Water vapor	945.0	26	60
10	Cirrus	1373.5	75	60
11	*Shortwave infrared 1*	*1613.7*	*143*	*20*
12	*Shortwave infrared 2*	*2202.4*	*242*	*20*

The italicized bands were used for spectral indices

where A_{dn} is final scaling factor from the internal slant range complex to the final 16-bit integer signed for slant range complex and unsigned for ground range detected, and α is local incidence angle.

Spectral Indices

Clay Index

Weathering can progress to great depths in crystalline basement rock areas, and accordingly, the permeability of aquifers formed in the basement rocks is enhanced compared to the overlying regolith (Jones 1985; Worthington et al. 2016). Because weathering can generate clay minerals that have deep absorption of reflectance in the shortwave infrared region (SWIR) due to the content of hydroxyl and/or water (Worthington et al. 2016; Rocchi et al. 2017), a simple image processing band ratio can be used to detect zones rich in clay minerals (Sabins 1999). The clay index (CI), calculated simply by rationing two SWIR band reflectances, $\rho_{\mathrm{SWIR1}}/\rho_{\mathrm{SWIR2}}$, has been a common method for this purpose, in which SWIR1 is a reference having large reflectance without absorption at 1.6 μm (band 11 of Sentinel-2A) and SWIR2 is the absorbed reflectance, which is typically at 2.2 μm (band 12) (Segal and Merin 1989; Sabins 1999; Ducart et al. 2016). The performance of this band ratio is degraded by the presence of vegetation cover because vegetation has a similar SWIR reflectance spectrum to clay minerals due to the abundance of water in leaves (Okada et al. 1993; Ouerghemmi et al. 2016; Bishop et al. 2017). Therefore, a large band ratio is generated by richness of both clay minerals and vegetation (Okada et al. 1993; Ducart et al. 2016).

To overcome this mixture problem and separate vegetated zones from clay-rich zones, the SWIR band ratio is normalized by a simple vegetation index, $\rho_{\mathrm{NIR}}/\rho_{\mathrm{Red}}$ (Jordan 1969) in which ρ_{Red} and ρ_{NIR} are reflectances at visible red (band 4 of Sentinel-2A) and narrow near infrared (band 8A), respectively. This normalized ratio, termed modified clay index (MCI), is formulated as:

$$\mathrm{MCI} = \frac{\rho_{\mathrm{SWIR1}}/\rho_{\mathrm{SWIR2}}}{\rho_{\mathrm{NIR}}/\rho_{\mathrm{Red}}} = \frac{\rho_{\mathrm{b11}} \cdot \rho_{\mathrm{b4}}}{\rho_{\mathrm{b12}} \cdot \rho_{\mathrm{b8A}}}, \quad (4)$$

where ρ_{b4}, ρ_{b8A}, ρ_{b11}, and ρ_{b12} are reflectances of the specified bands whose details are shown in Table 3. MCI is expected to be a large value in conditions with sparse vegetation and rich clay minerals without suppressing reflectance from background soils.

Vegetation Index

In arid and semiarid regions, vivid vegetation in the dry season suggests occurrence of groundwater at shallow depths. In addition to the clay index, abundance of vegetation cover is assessed by a vegetation index that can reduce the effect of reflectance from soils and increase the dynamic range of the vegetation signal. For this, the modified soil-adjusted vegetation index (MSAVI: Qi et al. 1994) is selected.

$$\mathrm{MSAVI} = \frac{2\rho_{\mathrm{b8A}} + 1 - \sqrt{(2\rho_{\mathrm{b8A}} + 1)^2 - 8(\rho_{\mathrm{b8A}} - \rho_{\mathrm{b4}})}}{2} \tag{5}$$

The superiority of MSAVI over the simple band ratio, $\rho_{\mathrm{NIR}}/\rho_{\mathrm{Red}}$, has been demonstrated for areas with sparse vegetation (Qi et al. 1994; Rondeaux et al. 1996; Matricardi et al. 2010; Petrakis et al. 2016), which is the case in the study area.

RESULTS AND DISCUSSION

Degree of Weathering from SAR Backscattering Coefficients

The degree of rock weathering over the study area was estimated from the σ^0 values of the ALOS PALSAR HH and HV polarization mode images ($\sigma^0_{\mathrm{L\_HH}}$ and $\sigma^0_{\mathrm{L\_HV}}$ in Fig. 3) and a Sentinel-1A VH polarization mode image ($\sigma^0_{\mathrm{C\_VH}}$ in Fig. 4). The subscripts L and C stand for the L and C bands, respectively. Common to the co- and cross-polarization ($\sigma^0_{\mathrm{L\_HH}}$ and $\sigma^0_{\mathrm{L\_HV}}$), the σ^0 of the dry season tended to be large in the mountainous zones and smaller mainly in the eastern flat zones. The large σ^0 also appeared locally in narrow strips in the small σ^0 zones. The fracture system in the study area was characterized well by the lineaments extracted from the multi-shaded SRTM DEM (Magaia et al. 2018). By overlaying the lineaments on the $\sigma^0_{\mathrm{L\_HH}}$ and $\sigma^0_{\mathrm{L\_HV}}$ maps, the $\sigma^0_{\mathrm{L\_HV}}$ was seen to be more correlated with the fracture zones than the $\sigma^0_{\mathrm{L\_HH}}$ because the thin strips with high $\sigma^0_{\mathrm{L\_HV}}$ overlapped generally with the lineaments, as shown in the insets of Figure 3. This correspondence probably originated from strong volume scattering due to abundant vegetation and high soil moisture content along the fracture zones.

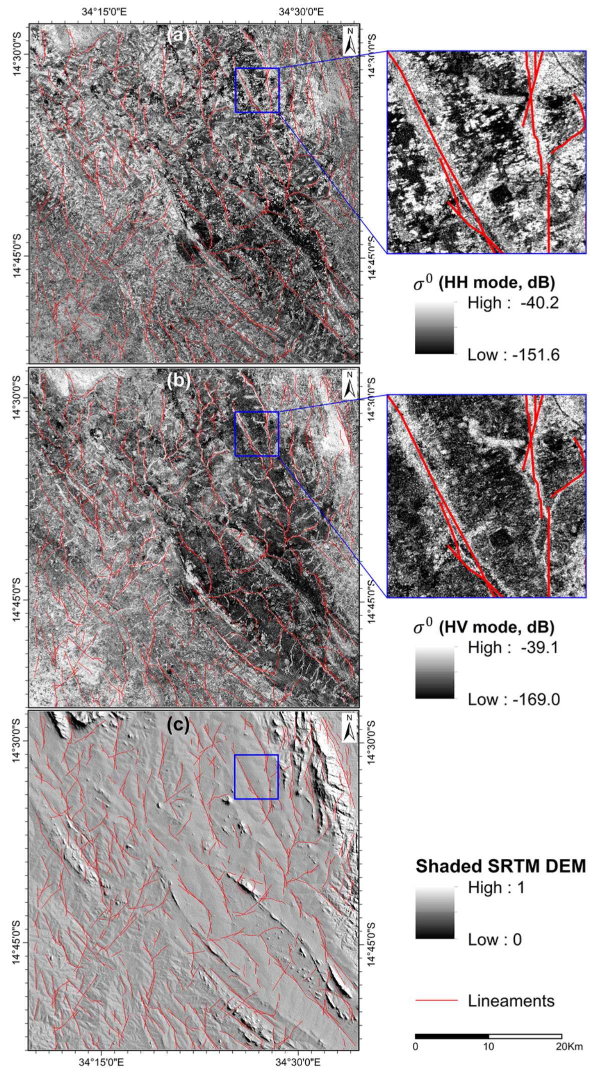

Figure 3. Surface backscattering coefficient images of a dry season scene of ALOS PALSAR (L band) at (**a**) HH and (**b**) HV polarization modes, and (**c**) shaded relief map of the SRTM DEM. All are overlaid with the lineaments extracted from multi-shaded SRTM DEM data (Magaia et al. 2018). The insets show positional correspondence between the zones of large surface backscattering coefficients and the lineaments.

Similar to the $\sigma^0_{\mathrm{L\_HV}}$ image, the large σ^0 zones corresponded with the lineaments in the $\sigma^0_{\mathrm{C\_VH}}$ images from Sentinel-1A (Fig. 4), but this correspondence became ambiguous in the rainy season scene (Fig. 4a) in which the difference in σ^0 between the lineaments and surrounding zones was smaller than in the dry season scene (Fig. 4b: see the insets for comparison).

Most lineaments were extracted from the valley features composed of streams and rivers (Magaia

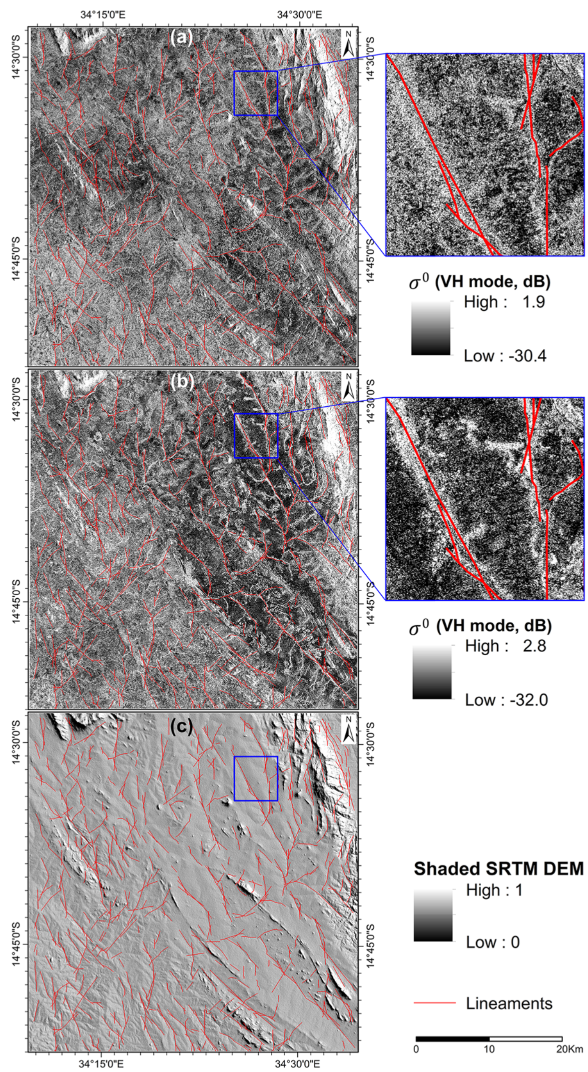

Figure 4. Surface backscattering coefficient images from Sentinel-1A (C band) at VH polarization mode from two scenes of (**a**) rainy and (**b**) dry seasons, and (**c**) shaded relief map of the SRTM DEM. All are overlaid with lineaments from Magaia et al. (2018). The insets show positional correspondence between the zones of large surface backscattering coefficients and the lineaments.

et al. 2018). The large σ^0 values in the valleys in both the $\sigma^0_{\mathrm{L\_HV}}$ and $\sigma^0_{\mathrm{C\_VH}}$ images signified higher soil moisture and/or the presence of higher vegetation activity than the neighboring zones, because soil moisture is retained selectively in tree canopies along valleys in arid and semiarid regions (Yu et al. 2018). Large σ^0 values appeared also in the mountainous zones where native vegetation was well preserved and this dense vegetation retained moisture. Owing to the abundance of moisture and vegetation, the dominance of volume scattering of microwaves was common to the L and C bands.

Because the positional correspondence between the large σ^0 zones and lineaments was best in the $\sigma^0_{\mathrm{L\_HV}}$ image due to the reduced effect of vegetation canopy in the longer wavelength and the dry season scene (as confirmed by the insets in Figs. 3 and 4), the $\sigma^0_{\mathrm{L\_HV}}$ image is discussed in detail later in this paper. First, to define quantitatively large or small σ^0 values, the $\sigma^0_{\mathrm{L\_HV}}$ values were classified into four classes using the first, second, and third quartiles as thresholds (Fig. 5a) and the resultant four classes were compared with the natural color composite of the Sentinel-2A image in the dry season (Fig. 5b). The most noteworthy feature is that the distributions of the MBA (35 km length and 8 km width) and the BBG-M (BBG with metasedimentary origin, CGS 2007) matched the smallest $\sigma^0_{\mathrm{L\_HV}}$ class, as shown in the eastern zone, colored blue in Figure 5a. This means that surface roughness in these areas is small (i.e., smooth with sparse vegetation). The sparse vegetation in these specific lithologic areas is confirmed by the bluish and brownish colors in the composite image (Fig. 5b), except for the thin and large $\sigma^0_{\mathrm{L\_HV}}$ zones along the major lineaments and streams, colored dark green.

To clarify the dependence of $\sigma^0_{\mathrm{L\_HV}}$ on lithologic unit, the histograms of $\sigma^0_{\mathrm{L\_HV}}$ values were drawn per lithologic unit (Fig. 6). The resultant histograms revealed that the $\sigma^0_{\mathrm{L\_HV}}$ values in the MBA and the BBG-M were biased toward small values, as shown by the black and blue histograms, and their means were the first two minima among the 10 lithologic units. These features corresponded with those that appear in Figure 5a. Conversely, the four lithologic units situated in the southwestern part, the Desaranhama granite porphyritic granite, the Desaranhama granite gneiss, the actinolite schist and amphibolite gneiss, and the equigranular tonalitic, quartz-feldspathic gneiss, bore large $\sigma^0_{\mathrm{L\_HV}}$ values as shown by the light brown, brown, green, and red histograms, respectively. The histograms of the quartzite and marble are not shown because the distribution of these units is very small in the study area, as mentioned above.

The two units of small σ^0, MBA and BBG-M, are weathered and are rich in clayey soils composed of colluvium clayey and red clayey soils in the top layer according to the 1:250,000 soil map from the National Center of Cartography and Remote Sens-

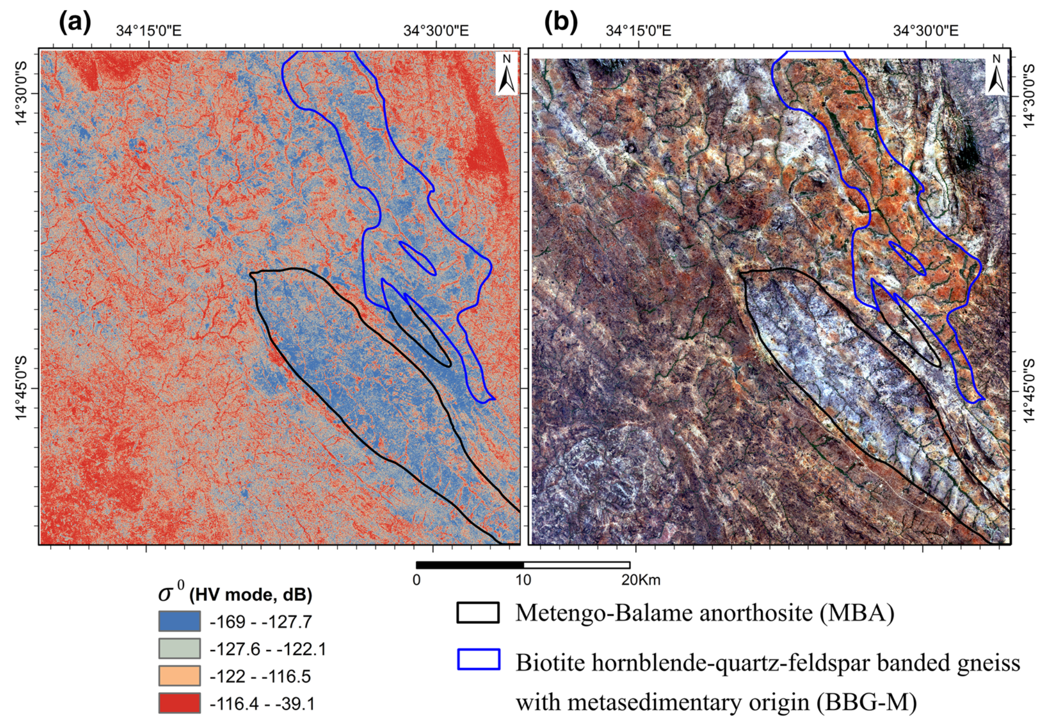

Figure 5. Comparison between (**a**) four classes based on magnitude of surface backscattering coefficient of the ALOS PALSAR image at HV mode and (**b**) natural color composition image from Sentinel-2A in which bands 4, 3, and 2 (see Table 3) were assigned to R, G, and B, respectively. Both images were derived from dry season scenes. The delineated zones with the smallest class in (**a**) almost overlap with the distributions of the MBA and the BBG-M. Vivid vegetation colored dark green in (**b**) is generally sparse in the whole area.

ing (CENACARTA). The former unit area is also characterized by low relief topography and loamy soils in the 1:250,000 geologic map by CGS (2007). Backscattering intensity in such clayey soils decreases with small roughness due to the dominance of specular reflection of microwaves (Hallikainen et al. 1985; Gharechelou et al. 2015). Long-term weathering smoothens rock surface by altering the rock into fine clay minerals (McCauley et al. 1982; Jones 1985; Dill 2016; Rocchi et al. 2017). These surface lithologic and topographic conditions can explain the small $\sigma^0_{\mathrm{L\_HV}}$ values in the two units. The degree of weathering is assessed in the next subsection from the viewpoint of clay richness in surface soils.

Discrimination of Weathered Zones and Assessment of Weathering Degree

To demonstrate the superiority of the proposed MCI over the simple clay index, CI, the two indices were applied to the Sentinel-2A images and the resultant maps were classified into four classes using the quartiles of their values (Fig. 7a and b), similar to the $\sigma^0_{\mathrm{L\_HV}}$ map of four classes (Fig. 5a). The clay richness increased from red (poorest) to light red, light blue, and blue (richest) classes in ascending order. A notable difference was that large CI values appeared in the mountain zones covered by thick vegetation (Fig. 7a), whereas the MCI values were small in these zones owing to limited soil reflectance (Fig. 7b). Another noted feature was that the mixing zones of vegetation and soil along the lineaments, in which vegetation is dominant as explained in section "Degree of Weathering from SAR Backscattering Coefficients" and shown in the MSAVI map below, were classified into clay-rich classes by CI (Figs. 3, 4 and 7a). The vegetation richness appeared correctly in the MCI map, as confirmed by the insets in Figure 7b.

To discriminate the weathered zones, the MCI map was compared with MSAVI map that was also classified into four classes by using the quartiles. The vegetation richness and activity increased from red (soils with sparse vegetation) to orange, light green,

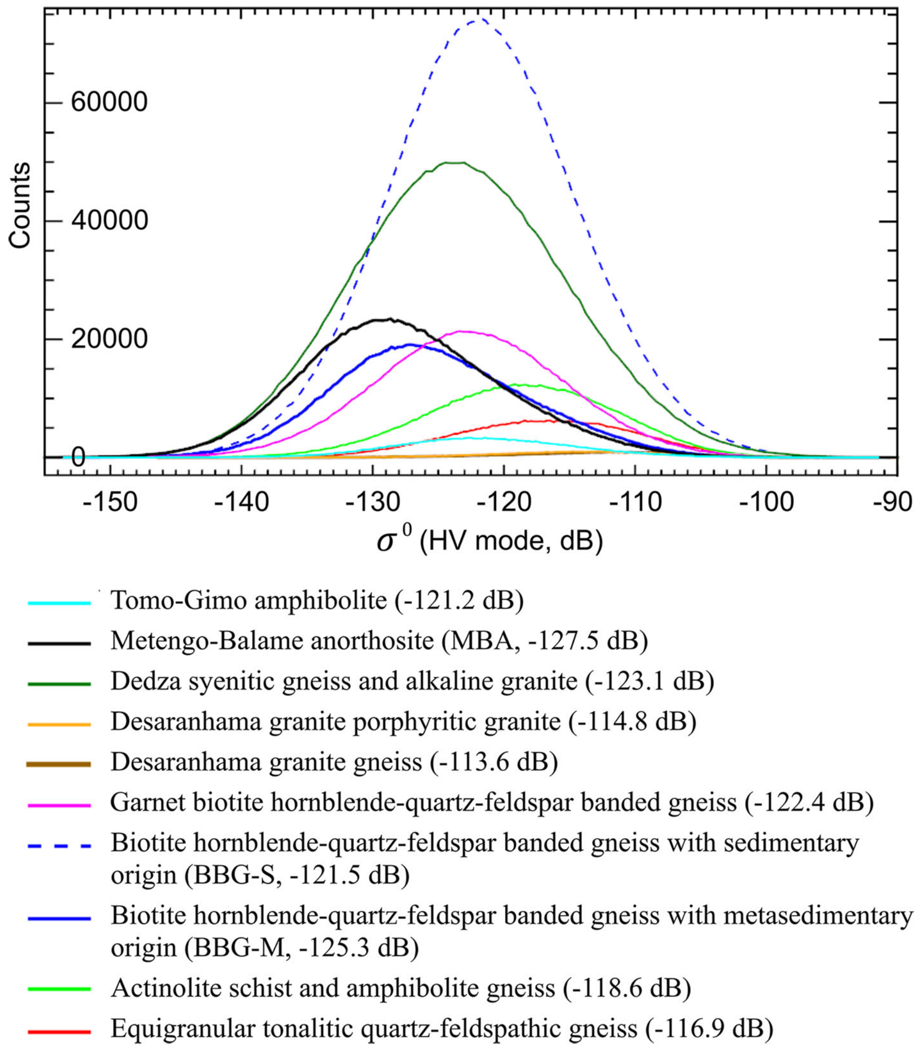

Figure 6. Histograms of surface backscattering coefficient values of the ALOS PALSAR image at HV mode in the 10 main lithologic units. The means per unit are also shown.

and green (rich and active vegetation) classes in ascending order (Fig. 7c). It is noteworthy that the above two lithologic units with small $\sigma^0_{\mathrm{L\_HV}}$ overlapped with the richest clay and poorest vegetation classes. This correspondence supported our interpretation of small $\sigma^0_{\mathrm{L\_HV}}$ due to the strong weathering and the resulting abundance of clay minerals.

Conversely, the poor clay classes colored in red and light red (Fig. 7b) corresponded well to the rich vegetation classes in green and light green (Fig. 7c). This agreement was confirmed in the southwestern and northeastern mountainous zones. Owing to the volume scattering of vegetation, the $\sigma^0_{\mathrm{L\_HV}}$ took large values in these areas as the third and fourth classes (Fig. 5a).

Superimposition of the lineaments on the two spectral index maps highlighted that the lineaments overlapped well with the narrow zones of the rich vegetation classes (green and light green classes) and the large $\sigma^0_{\mathrm{L\_HV}}$ zones (as shown in the insets in Figs. 3b and 7c). This confirmed that the lineaments corresponded chiefly to fracture zones where most groundwater was stored at shallow levels, as found by Magaia et al. (2018).

Another noted feature was that two major NNW-trending faults and several NNE- and NE-trending inferred faults were distributed in the two

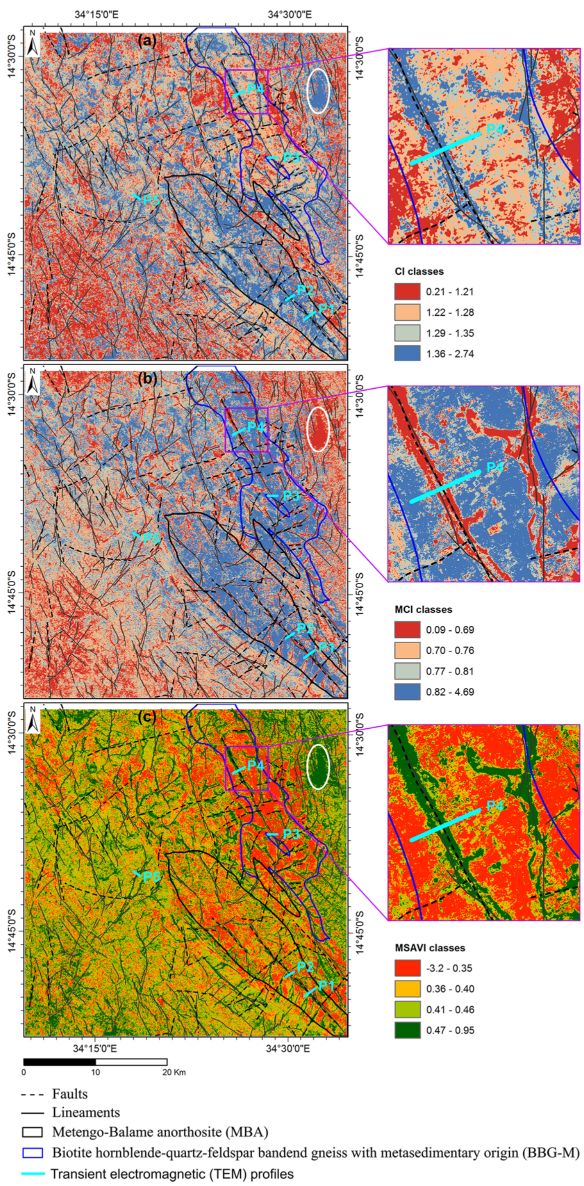

◀**Figure 7.** Comparison of two maps produced by (**a**) the simple clay index (CI) and (**b**) the modified clay index (MCI), which were classified into four classes by the quartiles in which clay richness increases from red (poorest) to light red, light blue, and blue (richest) classes in ascending order. (**c**) Modified soil-adjusted vegetation index (MSAVI) map, also classified into four classes in which the red class is bare soil with sparse vegetation and vegetation activity increases toward orange, light green, and green (richest and active) classes. All maps are overlaid with the lineaments, similar to Figures 3 and 4. Positional correspondence between the lineaments and the three spectral indices is verified in the insets. The zones along the lineaments are relatively rich in vegetation, and therefore, the clay index must be low and MSAVI must be high. White ellipses outline the mountain zone covered by thick vegetation, in which the clay index must also be low, to demonstrate the superiority of MCI over CI. Locations of five TEM profiles across the lineaments for resistivity cross sections are also included.

lithologic units with small $\sigma^0_{\mathrm{L\_HV}}$ and rich clay content, and the units were located in the large density zones of faults and lineaments (Fig. 8). The faults are shear fractures with large vertical displacement, but the lineaments originated from both shear fractures and tensile fractures such as joints and fissures that were limited in length, depth, and rock fragmentation. Rock fracturing by faults advances the weathering of basement rocks more effectively and strongly than tensile fractures (National Research Council 1996; Owen et al. 2007; Singhal and Gupta 2010), and develops thick regolith with large porosity and permeability (Chilton and Foster 1995). However, such regolith contains many clay minerals, such as kaolinite, that reduce permeability at shallow depths (Jones 1985; Chilton and Foster 1995; Dill 2016). The faults and part of the lineaments increase the permeability of the basement aquifers below the surface clay layers.

Validation of Groundwater Potential Zones

Based on the above results, the high potential for groundwater resources was estimated in the two lithologic units (MBA and BBG-M) with small $\sigma^0_{\mathrm{L\_HV}}$ and the narrow zones of large $\sigma^0_{\mathrm{L\_HV}}$ along the lineaments with a large vegetation index. To verify this estimation, a 1:1,000,000 hydraulic map prepared by DNA (1987), the well survey data, and the geophysical survey transient electromagnetic (TEM) dataset from Magaia et al. (2018) were used. The map classified the study area into four hydraulic classes. Here, MBA and BBG-M were ranked as relatively permeable classes, B3 for MBA and C1 for BBG-M (Fig. 9). The permeability of the sedimentary unit, BBG-S, having similar lithology to BBG-M, varied with location, C1 in the northwest, C2 in the south, and C3 in the northwest, middle and southern mountain zones (Fig. 9).

Although rich vegetation was estimated for the C2 and C3 zones from the large MSAVI values and relatively large σ^0 values in both L and C band SAR images, the groundwater potential of these zones was ranked low. Their mountainous topography with steep slopes, which induce high run-off from the

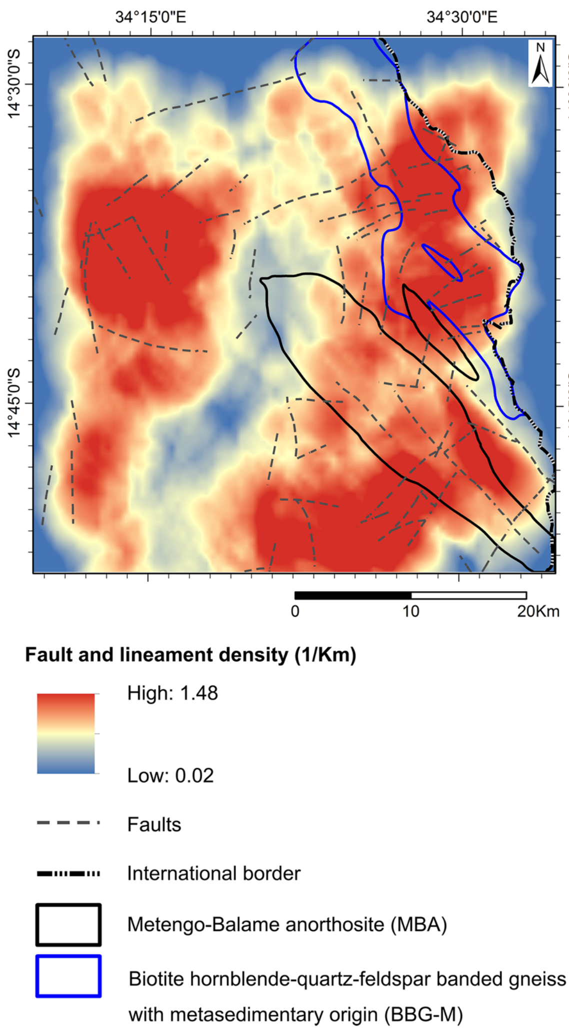

Figure 8. Density map of faults and lineaments highlighting large density zones in and around the lithologic units MBA and BBG-M with small $\sigma^0_{\mathrm{L\_HV}}$. The fault and lineament data are from DNG (2006) and Magaia et al. (2018), respectively.

rains and prevent rain infiltration and development of a thick weathering layer, is a plausible reason for this low potential.

Another verification was tried for estimating the weathered zone thickness and the groundwater potential using existing data of well drilling depth and potential yield (Fig. 10). In addition to strong heterogeneities in the aquifer structures in the study area, the difference in the season of drilling the wells and the uncertainties in correctly determining the potential yield might be reasons for the weak correlation of the results with the verification data. Nevertheless, the results can be used as general or relative indicator of the thickness of the weathered zone. The mean depth was 34 m, and the minimum potential yield was 900 l/h. Therefore, the aquifers targeted in the study area were the places that could provide groundwater at least 900 l/h throughout the year below about 34 m depth.

Three classes were set to each of the depth and yield data: shallow (15.5–30 m), moderate (30.1–37.3 m), and deep (37.4–56 m) classes and low (900–1400 l/h), intermediate (1401–2400 l/h), and high (2401–7000 l/h) yield classes using the tertiles of value distribution (i.e., value intervals smaller than the first, within the first to second, and larger than the second tertiles). These classes were overlaid on the hydraulic map (Fig. 9). Because no geologic data were recorded and no well loggings were implemented at all the well locations, the bottom depth of regolith could not be accessed. However, the mean well depth was close to the mean thickness of regolith, 27 m, measured by borehole surveys in the regolith-rich aquifers in Malawi located near and under similar geologic settings to this study area (data from Table 2 in Wright 1992). The well bottoms in this study area were set in the fractured zones above the intact rocks from which groundwater can be pumped up efficiently. Therefore, the depth range from the ground surface to the well bottom can be regarded roughly as the thickness of regolith.

The 15 wells in BBG-M, which was identified as rich in clay by σ^0 and MCI, had a high ratio of moderate and deep depth classes; 80% and 87% of them were ranked as intermediate and high potential yield classes, respectively. Despite having similar lithology as BBG-M, the BBG-S areas were ranked as low hydraulic classes (C1 to C3) with moderate clay content and sparse to moderate vegetation activity, and 65% of the 54 wells in the areas were moderate and deep depth classes, and 59% of wells were intermediate and high potential yield classes. These reductions in percentages were attributed to poor development of the regolith because of the smaller fault density in BBG-S. In addition to the effect of fault fracturing, the difference in mineral composition will determine the development of weathering (e.g., Ehlen 2002; Worthington et al. 2016; Rocchi et al. 2017).

For another clay-rich unit, MBA, the verification was difficult because there were only two recorded wells in it: a shallow depth (21 m) with low potential yield (1050 l/h) and a moderate depth (35 m) with high yield (4500 l/h). However, this unit

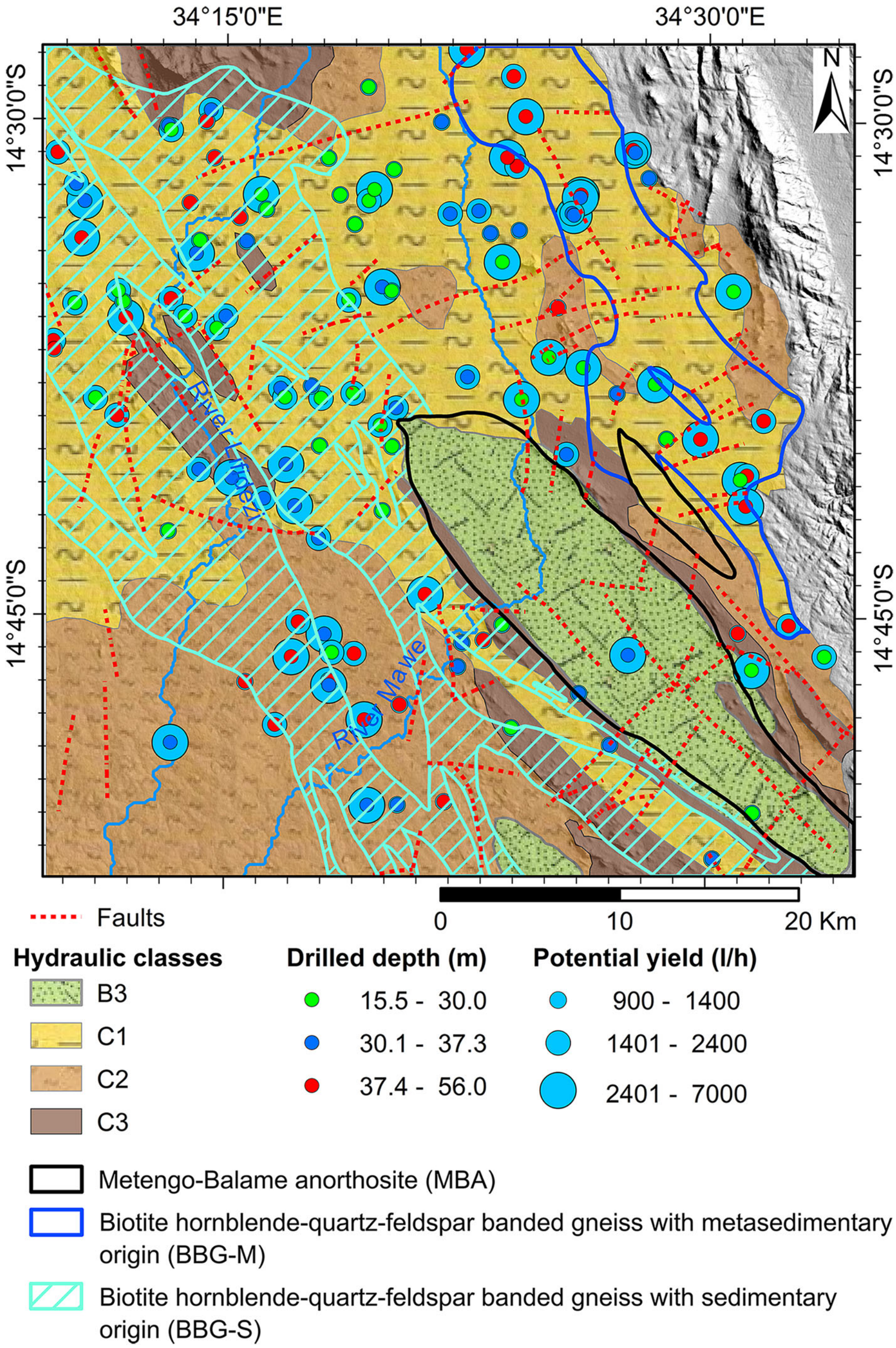

Figure 9. Hydraulic classes in the study area, modified from DNA (1987) overlaid on a SRTM DEM shaded relief backdrop. The classes are B3 representing the highest permeability in the study area that has well-fractured aquifers with the highest productivity (3–10 m^3/h), C1 representing low permeability that has continuous or discontinuous local aquifers with productivity limited to less than 5 m^3/h, C2 representing very low permeability with very limited groundwater occurrence (< 3 m^3/h), and C3 representing impermeable and devoid of groundwater occurrence, located mainly in mountainous topography. Well depth and potential yield data were from the Water and Sanitation Division of Tete Province (DAS-Tete). The fault data are from DNG (2006).

was evaluated as the most permeable and productive (B3) in the area. This feature must be attributable to the highest fault density (Fig. 8) and the flat topography of the unit as evidenced by the small σ^0.

To clarify the utility of $\sigma^0_{\mathrm{L\_HV}}$ and MCI for estimating weathering degree, a correlation of the bottom well depth with $\sigma^0_{\mathrm{L\_HV}}$ and MCI at the well location was examined as shown in Figures 11 and 12. Two nonparametric tests, the Spearman (r_s) and Kendall (τ) rank correlation coefficients, which have been widely used for data distributions whose normality is not verified in either or both the variables as in this study, were implemented to check the statistical meaning of the association. The tests showed that both correlations were weak (Table 4). The correlation between the bottom well depth and $\sigma^0_{\mathrm{L\_HV}}$ was statistically nonsignificant because the primary probability condition, $p \leq 0.05$, was not satisfied in either test. The correlation between the bottom well depth and MCI was statistically significant. Although the correlations were weak, the bottom depth (i.e., thickness of weathered zone) tended to increase roughly with decreasing $\sigma^0_{\mathrm{L\_HV}}$ and increasing MCI. This general trend suggests that the backscattering coefficient and clay index can be related to weathering degree. For example, the range of regolith thickness was roughly estimated using the regression lines and the upper and lower boundaries of the 75% and 95% prediction intervals.

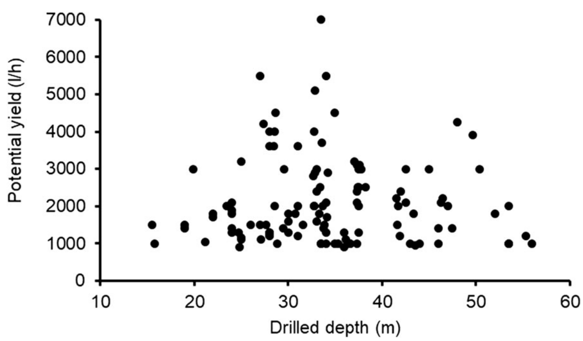

Figure 10. Relationship between well bottom depth and potential yield of the groundwater wells shown in Figure 9.

The lack of correlation between bottom depth and potential yield (Fig. 10) indicates that the regolith thickness is not the only factor controlling groundwater occurrence. As mentioned above, fault fracturing was probably one of the controlling factors. To confirm this inference, a scatterplot between distance to nearest lineament from each well location and potential yield was drawn (Fig. 13). Although their correlation was very weak, similar to Figures 11 and 12, the upper limit of potential yield tended roughly to increase with proximity to lineaments. This trend can explain the high potential yield in the shallow wells even in the limited groundwater occurrence class C2 in Figure 9. Therefore, the fracture zones that partially appeared as lineaments in the study area can provide a field for groundwater storage and preferential groundwater flow through the development of weathering and/or groundwater paths in the bedrocks. The other control factors of potential yield that weaken the correlations in Figures 11, 12, and 13 may be fracture network and dike occurrence.

Moreover, the resistivity (ρ) distributions derived by inversion analysis of the TEM dataset were used for the third verification of the weathered zones

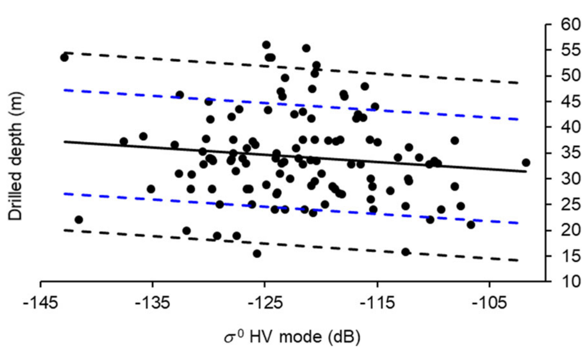

Figure 11. Correlation between bottom well depth and ALOS PALSAR backscattering coefficient at the HV mode ($\sigma^0_{\mathrm{L\_HV}}$) at the well locations. The regression line (the solid line) and the upper and lower boundaries of the 75% and 95% prediction intervals (blue and black dashed lines, respectively) of the trend line are overlaid.

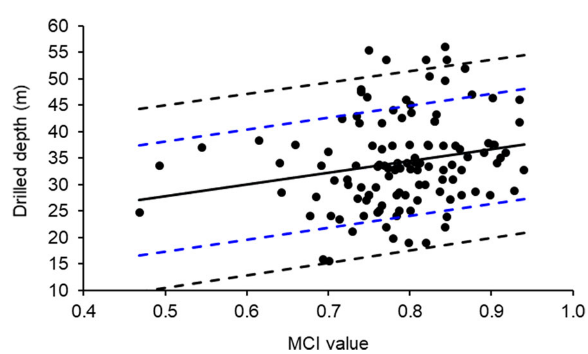

Figure 12. Correlation between bottom well depth and MCI value at the well locations. The regression line (the solid line) and the upper and lower boundaries of the 75% and 95% prediction intervals (blue and black dashed lines, respectively) of the trend line are overlaid.

Table 4. Results of Spearman and Kendall rank tests to check the statistical significance of the correlations of the bottom well depth with the surface backscattering coefficient and modified clay index

Variables	Distribution	Spearman		Kendall	
		r_s	p	τ	p
Drilled depth and $\sigma^0_{\mathrm{L\_HV}}$	Tailed and normal	− 0.11	0.25	− 0.08	0.22
Drilled depth and MCI	Tailed and tailed	0.24	0.008	0.16	0.009

Types of the underlying variable distributions are also shown

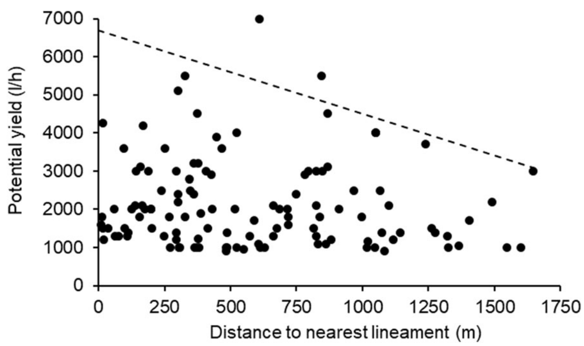

Figure 13. Relationship between distance to the nearest lineament from each well location and the potential yield. The dashed curve stands for the approximate upper limit of the potential yield.

specified by $\sigma^0_{\mathrm{L\_HV}}$ and MCI. Five TEM profiles over the study area (Fig. 7) were selected as representative zones across the narrow strips of large σ^0, high activity vegetation zone in widely small σ^0, clay-rich zone. Four of the profiles were across the main axes of MBA (profiles 1 and 2) with the hydraulic class B3 and BBG-M (profiles 3 and 4) with C1. Profile 5 in BBG-S with C1 was to check a formation of weathered zone in a rich vegetation zone outside the two clay-rich zones. Four irregular and discontinuous layers were discriminated by the ρ values (Fig. 14).

Layer I is formed near the surface in all the profiles due to the formation of clay minerals by intense weathering and overlies thick layer III in general near the fracture zones. Layer II intercalates with layer III and becomes more noticeable at both ends of every profile. An effect of lineaments on the groundwater storage by increasing permeability of the underlying rocks is well marked in profiles 1, 3, 4, and 5, because layer III is distributed extensively and thickly around the fracture zones. In the zones around them, MSAVI and MCI values become high and low, respectively, because of active vegetation. Although layer I tends to be thick toward the lineament in profile 2, layer III appears apart from the lineament. This is a case of non-correlation of the main weathered layer with the lineaments.

The five profiles revealed variability in thickness and location of the main weathered layer (layer III). However, it tends to be thick toward the lineaments in the middle profiles where the σ^0 values become large due to the active vegetation. The intense weathering along the lineaments must cause much groundwater storage, and consequently, the wells with large potential yield are located generally near the lineaments as shown in Figure 13.

CONCLUSIONS

This study aimed to develop a remote sensing-based potential mapping of groundwater resources in crystalline rock areas in a semiarid region through a combination of surface backscattering coefficients of L and C band SAR images (ALOS PALSAR and Sentinel-1A images, respectively) and two spectral indices, clay and vegetation, derived from an optical sensor image (Sentinel-2A image). The degree of weathering in a regolith-rich area in central Mozambique was estimated by the combination because advanced weathering can form an excellent aquifer with large porosity and permeability. Two types of high potential zones were clarified. The first type comprised zones of high weathering degree with high density of faults and lineaments, which were characterized by small surface backscattering coefficients (i.e., having smooth Earth surface and being rich in clay minerals owing to advanced weathering). The second type comprised narrow zones along lineaments where surface backscattering coefficients of the cross-polarized images were large in both the L and C band images. From these images, high vegetation vigor that induces large volume scattering throughout the year was inferred. Using data from 118 groundwater wells on bottom depth

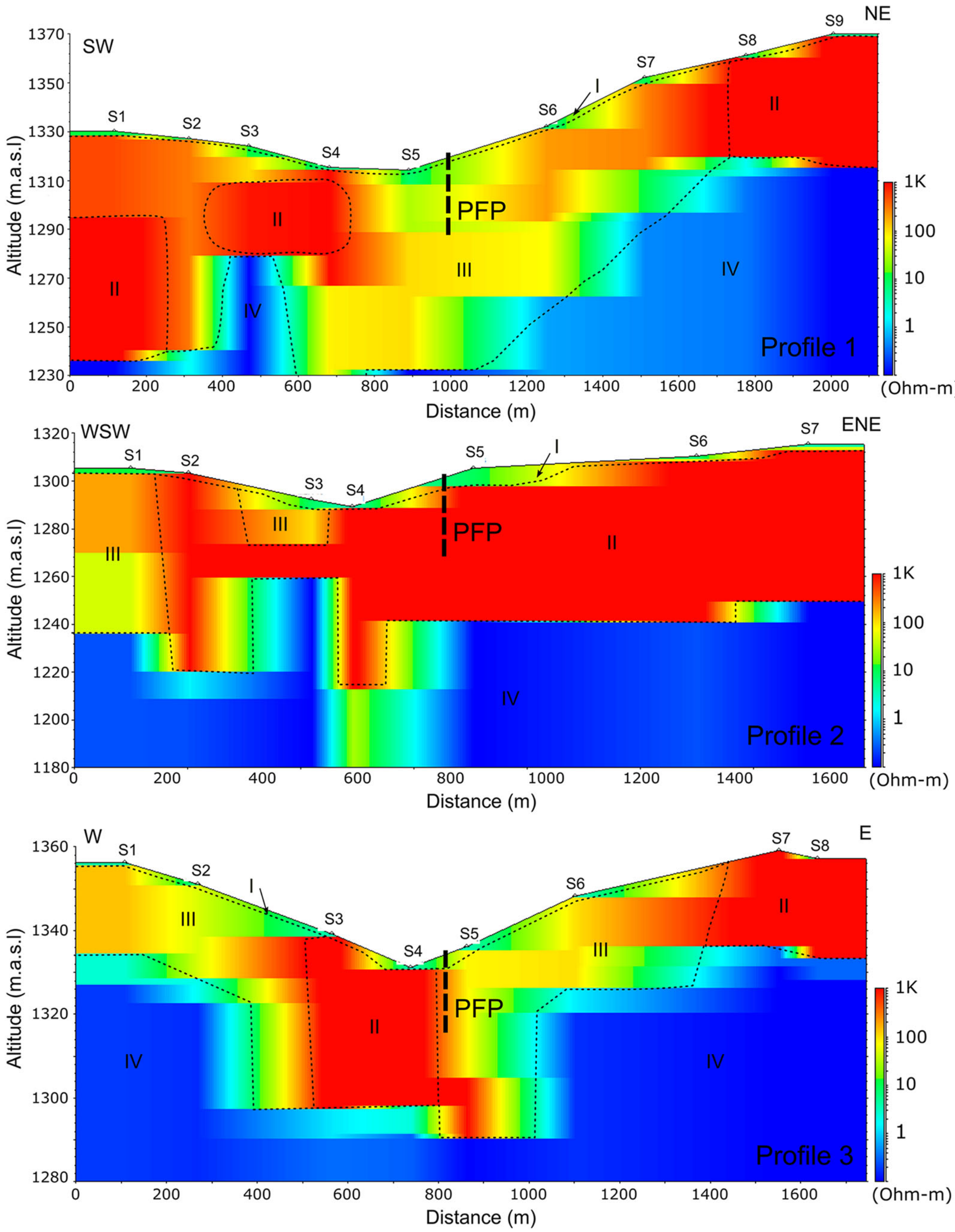

Figure 14. Cross sections of TEM resistivity produced by an inversion analysis of the TEM dataset by Magaia et al. (2018), along profiles 1 and 2 in MBA, profiles 3 and 4 in BBG-M, and profile 5 in BBG-S. The resistivities were classified into four value ranges (I to IV layer): I, a top layer of alternating sediments with low to moderate ρ (4–12 Ωm); II, fractured, less weathered, and highly resistive layer with low porosity ($\rho \geq 400$ Ωm); III, fractured and weathered layer with high potential of groundwater storage (ρ = 10–300 Ωm); and IV, located at the bottom of profiles ($\rho \leq 10$ Ωm) with low ρ resulting from accumulation of clay mineral, iron oxides, and/or graphite in deep zones (Magaia et al. 2018). PFP stands for possible fracture position inferred from the lineament data by Magaia et al. (2018). Profile locations are shown in Figure 7.

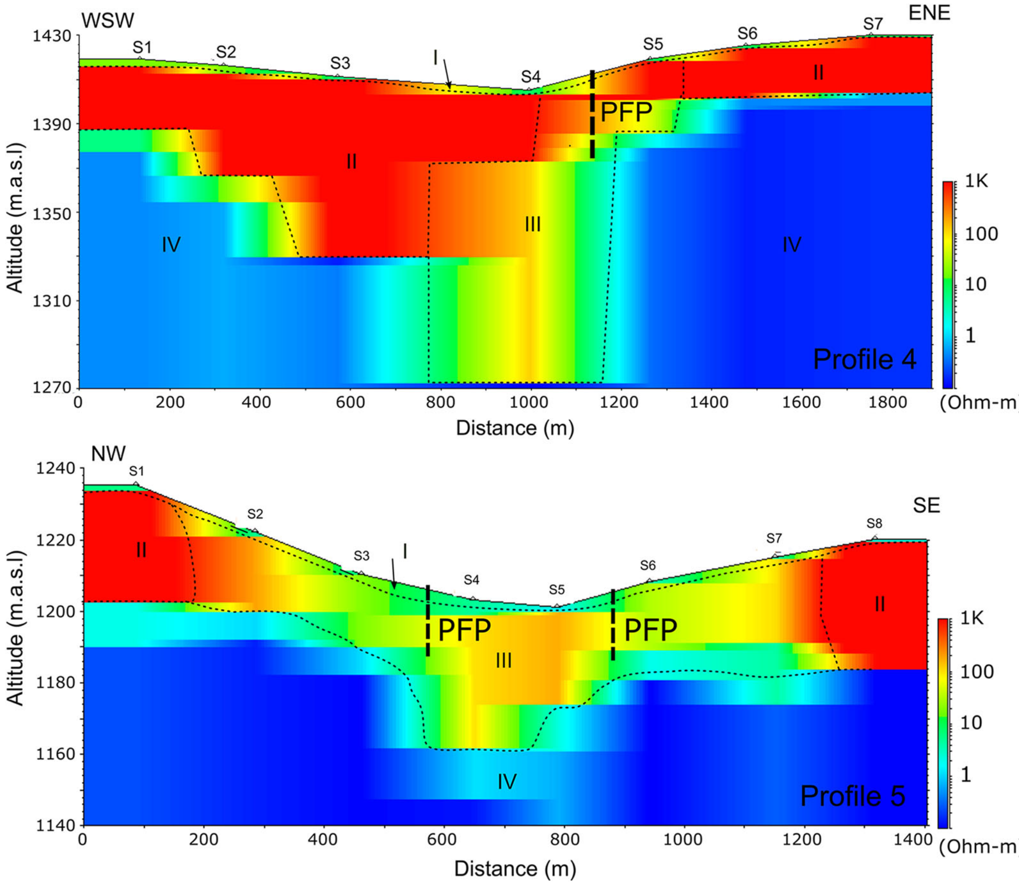

Figure 14. continued.

and potential yield, we demonstrated the plausibility of the two types of groundwater occurrence as follows. The bottom depth was considered to be related to thickness of weathered zone based on the general pumping style in the study area. Overall, the potential yields tended to increase as the wells approached the lineaments for the second type, and the bottom depths were likely to increase with decreasing backscattering coefficients and increasing clay index values for the first type.

Consequently, the effectiveness of the above combination was demonstrated for remote sensing-based mapping of groundwater potential in semiarid regions without detailed water investigation data as a first-pass approach before detailed surface geophysical surveys. More advanced SAR data analysis, spectral analyses for clay and vegetation abundances, and detection of fracture-related topographic features are our next study aims. We will use these proposed techniques to enhance the estimation accuracy of weathering degree and regolith thickness, and the reliability of groundwater potential mapping in an efficient and cost-effective way.

ACKNOWLEDGMENTS

We thank the Japan International Cooperation Agency (JICA) for supporting this study and the Water and Sanitation Division of Tete Province (DAS-Tete) in Mozambique for providing the groundwater well data. This work was partially supported by JSPS KAKENHI (Grant Number 18H01924). Sincere thanks are extended to two anonymous reviewers and Editor-in-Chief Dr. John Carranza for their valuable comments and suggestions that helped improve the clarity of the manuscript.

REFERENCES

Acworth, R. I. (1987). The development of crystalline basement aquifers in a tropical environment. *Quarterly Journal of Engineering Geology and Hydrogeology, 20*(4), 265–272. https://doi.org/10.1144/GSL.QJEG.1987.020.04.02.

Asf, DAAC. (2015). ALOS PALSAR_radiometric_terrain_corrected_high_res; includes material JAXA/METI 2007. Accessed through ASF DAAC,https://www.asf.alaska.edu, August 25, 2017. https://doi.org/10.5067/z97hfcnkr6va.

Bishop, J. L., Michalski, J. R., & Carter, J. (2017). Remote detection of clay minerals. *Developments in Clay Science, 8,* 482–514. https://doi.org/10.1016/B978-0-08-100355-8.00014-X.

CGS. (2007). *Map explanation: Sheets Furancungo (1433) and Ulongue (1434), scale 1:250,000*. Maputo: Ministério dos Recursos Minerais, Direcção Nacional de Geologia.

Chilton, P. J., & Foster, S. S. D. (1995). Hydrogeological characterisation and water-supply potential of basement aquifers in Tropical Africa. *Hydrogeology Journal, 3*(1), 36–49. https://doi.org/10.1007/s100400050061.

Chirindja, F. J., Dahlin, T., & Juizo, D. (2017). Improving the groundwater-well siting approach in consolidated rock in Nampula Province. *Mozambique. Hydrogeology Journal, 25*(5), 1423–1435. https://doi.org/10.1007/s10040-017-1540-1.

Corgne, S., Magagi, R., Yergeau, M., & Sylla, D. (2010). An integrated approach to hydro-geological lineament mapping of a semi-arid region of West Africa using Radarsat-1 and GIS. *Remote Sensing of Environment, 114*(9), 1863–1875. https://doi.org/10.1016/j.rse.2010.03.004.

Dill, H. G. (2016). Kaolin: Soil, rock and ore: From the mineral to the magmatic, sedimentary and metamorphic environments. *Earth-Science Reviews, 161,* 16–129. https://doi.org/10.1016/j.earscirev.2016.07.003.

DNA. (1987). *Carta hidrogeológica escala 1:1,000,000 1ª edição*. Maputo: Ministério de Construção e Águas, Direcção Nacional de Águas.

DNG. (2006). *Geological sheet 1:250,000, No. 1434*. Maputo: Ministério dos Recursos Minerais, Direcção Nacional de Geologia.

Ducart, D. F., Silva, A. M., Toledo, C. L. B., & de Assis, L. M. (2016). Mapping iron oxides with Landsat-8/OLI and EO-1/Hyperion imagery from the Serra Norte iron deposits in the Carajás Mineral Province, Brazil. *Brazilian Journal of Geology, 46*(3), 331–349. https://doi.org/10.1590/2317-4889201620160023.

Ehlen, J. (2002). Some effects of weathering on joints in granitic rocks. *CATENA, 49*(1–2), 91–109. https://doi.org/10.1016/S0341-8162(02)00019-X.

Engman, E. T. (1991). Application of microwave remote sensing of soil moisture for water resources and agriculture. *Remote Sensing of Environment, 35*(2–3), 213–226. https://doi.org/10.1016/0034-4257(91)90013-V.

Foster, S. (2012). Hard-rock aquifers in tropical regions: Using science to inform development and management policy. *Hydrogeology Journal, 20*(4), 659–672. https://doi.org/10.1007/s10040-011-0828-9.

Gharechelou, S., Tateishi, R., & Sumantyo, J. T. S. (2015). Interrelationship analysis of L-band backscattering intensity and soil dielectric constant for soil moisture retrieval using PALSAR data. *Advances in Remote Sensing, 4*(1), 15–24. https://doi.org/10.4236/ars.2015.41002.

Hallikainen, M. T., Ulaby, F. T., Dobson, M. C., El-Rayes, M. A., & Wu, L.-K. (1985). Microwave dielectric behavior of wet soil-part I: Empirical models and experimental observations. *IEEE Transactions on Geoscience and Remote Sensing, GE-23*(1), 25–34. https://doi.org/10.1109/tgrs.1985.289497.

Jones, M. J. (1985). The weathered zone aquifers of the basement complex areas of Africa. *Quarterly Journal of Engineering Geology and Hydrogeology, 18*(1), 35–46. https://doi.org/10.1144/GSL.QJEG.1985.018.01.06.

Jordan, C. F. (1969). Derivation of Leaf-Area Index from quality of light on the forest floor. *Ecology, 50*(4), 663–666. https://doi.org/10.2307/1936256.

Koch, M., & Mather, P. M. (1997). Lineament mapping for groundwater resource assessment: A comparison of digital Synthetic Aperture Radar (SAR) imagery and stereoscopic Large Format Camera (LFC) photographs in the Red Sea Hills, Sudan. *International Journal of Remote Sensing, 18*(7), 1465–1482. https://doi.org/10.1080/014311697218223.

Kornelsen, K. C., & Coulibaly, P. (2013). Advances in soil moisture retrieval from synthetic aperture radar and hydrological applications. *Journal of Hydrology, 476,* 460–489. https://doi.org/10.1016/j.jhydrol.2012.10.044.

Laur, H., Bally, P., Meadows, P., Sanchez, J., Schaettler, B., Lopinto, E., et al. (2004). *ERS SAR calibration: Derivation of the backscattering coefficient σ0 in ESA ERS SAR PRI products*. *ESA Document No. ES-TN-RE-PM-HL09, Issue 2, Rev. 5f.* Noordjiwk, The Netherlands. https://earth.esa.int/documents/10174/13019/ers_sar_calibration_issue2_5f.pdf.

Magaia, L. A., Goto, T., Masoud, A. A., & Koike, K. (2018). Identifying groundwater potential in crystalline basement rocks using remote sensing and electromagnetic sounding techniques in central Western Mozambique. *Natural Resources Research, 27*(3), 275–298. https://doi.org/10.1007/s11053-017-9360-5.

Matricardi, E. A. T., Skole, D. L., Pedlowski, M. A., Chomentowski, W., & Fernandes, L. C. (2010). Assessment of tropical forest degradation by selective logging and fire using Landsat imagery. *Remote Sensing of Environment, 114*(5), 1117–1129. https://doi.org/10.1016/j.rse.2010.01.001.

McCauley, J. F., Schaber, G. G., Breed, C. S., Grolier, M. J., Haynes, C. V., Issawi, B., et al. (1982). Subsurface valleys and geoarcheology of the Eastern Sahara revealed by Shuttle Radar. *Science, 218*(4576), 1004–1020. https://doi.org/10.1126/science.218.4576.1004.

Miranda, N., & Meadows, P. J. (2015). *Radiometric calibration of S-1 level-1 products generated by the S-1 IPF. Ref. ESA-EOPG-CSCOP-TN-0002, Issue 1, Rev. 0*. https://sentinel.esa.int/documents/247904/685163/S1-Radiometric-Calibration-V1.0.pdf.

Mueller-Wilm, U. (2017). *S2 MPC: Sen2Cor Software Release Note. Ref. S2-PDGS-MPC-L2A-SRN-V2.4.0, Issue 02*. ESA. http://step.esa.int/thirdparties/sen2cor/2.4.0/Sen2Cor_240_Documenation_PDF/S2-PDGS-MPC-L2A-SRN-V2.4.0.pdf.

National Research Council (1996). *Rock fractures and fluid flow: Contemporary understanding and applications*. Washington, DC: The National Academies Press. https://doi.org/10.17226/2309.

Okada, K., Segawa, K., & Hayashi, I. (1993). Removal of the vegetation effect from LANDSAT TM and GER imaging spectroradiometer data. *ISPRS Journal of Photogrammetry and Remote Sensing, 48*(6), 16–27. https://doi.org/10.1016/0924-2716(93)90052-O.

Ouerghemmi, W., Gomez, C., Naceur, S., & Lagacherie, P. (2016). Semi-blind source separation for the estimation of the clay content over semi-vegetated areas using VNIR/SWIR hyperspectral airborne data. *Remote Sensing of Environment, 181,* 251–263. https://doi.org/10.1016/J.RSE.2016.04.013.

Owen, R., Maziti, A., & Dahlin, T. (2007). The relationship between regional stress field, fracture orientation and depth of weathering and implications for groundwater prospecting in crystalline rocks. *Hydrogeology Journal, 15*(7), 1231–1238. https://doi.org/10.1007/s10040-007-0224-7.

Petrakis, R., Wu, Z., McVay, J., Middleton, B., Dye, D., & Vogel, J. (2016). Vegetative response to water availability on the San Carlos Apache Reservation. *Forest Ecology and Management, 378,* 14–23. https://doi.org/10.1016/j.foreco.2016.07.012.

Qi, J., Chehbouni, A., Huete, A. R., Kerr, Y. H., & Sorooshian, S. (1994). A modified soil adjusted vegetation index. *Remote Sensing of Environment, 48*(2), 119–126. https://doi.org/10.1016/0034-4257(94)90134-1.

Rees, W. G. (2001). *Physical principles of remote sensing* (2nd ed.). Cambridge: Cambridge University Press. https://doi.org/10.1017/CBO9780511812903.

Rocchi, I., Coop, M. R., & Maccarini, M. (2017). The effects of weathering on the physical and mechanical properties of igneous and metamorphic saprolites. *Engineering Geology, 231,* 56–67. https://doi.org/10.1016/j.enggeo.2017.10.003.

Rondeaux, G., Steven, M., & Baret, F. (1996). Optimization of soil-adjusted vegetation indices. *Remote Sensing of Environment, 55*(2), 95–107. https://doi.org/10.1016/0034-4257(95)00186-7.

Rosenqvist, A., Shimada, M., Ito, N., & Watanabe, M. (2007). ALOS PALSAR: A pathfinder mission for global-scale monitoring of the environment. *IEEE Transactions on Geoscience and Remote Sensing, 45*(11), 3307–3316. https://doi.org/10.1109/TGRS.2007.901027.

Sabaghy, S., Walker, J. P., Renzullo, L. J., & Jackson, T. J. (2018). Spatially enhanced passive microwave derived soil moisture: Capabilities and opportunities. *Remote Sensing of Environment, 209,* 551–580. https://doi.org/10.1016/j.rse.2018.02.065.

Sabins, F. (1999). Remote sensing for mineral exploration. *Ore Geology Reviews, 14*(3–4), 157–183. https://doi.org/10.1016/S0169-1368(99)00007-4.

Saepuloh, A., Koike, K., Urai, M., & Sri Sumantyo, J. T. (2015). Identifying surface materials on an active volcano by deriving dielectric permittivity from polarimetric SAR data. *IEEE Geoscience and Remote Sensing Letters, 12*(8), 1620–1624. https://doi.org/10.1109/LGRS.2015.2415871.

Segal, D. B., & Merin, I. S. (1989). Successful use of Landsat Thematic Mapper data for mapping hydrocarbon microseepage-induced mineralogic alteration, Lisbon Valley, Utah. *Photogrammetric Engineering and Remote Sensing, 55*(8), 1137–1145.

Shaban, A., Khawlie, M., & Abdallah, C. (2006). Use of remote sensing and GIS to determine recharge potential zones: The case of Occidental Lebanon. *Hydrogeology Journal, 14*(4), 433–443. https://doi.org/10.1007/s10040-005-0437-6.

Shi, J., Wang, J., Hsu, A. Y., O'Neill, P. E., & Engman, E. T. (1997). Estimation of bare surface soil moisture and surface roughness parameter using L-band SAR image data. *IEEE Transactions on Geoscience and Remote Sensing, 35*(5), 1254–1266. https://doi.org/10.1109/36.628792.

Shimada, M., Isoguchi, O., Tadono, T., & Isono, K. (2009). PALSAR radiometric and geometric calibration. *IEEE Transactions on Geoscience and Remote Sensing, 47*(12), 3915–3932. https://doi.org/10.1109/TGRS.2009.2023909.

Singhal, B. B. S., & Gupta, R. P. (2010). *Applied hydrogeology of fractured rocks* (2nd ed.). Berlin: Springer. https://doi.org/10.1007/978-90-481-8799-7.

Small, D., & Schubert, A. (2008). *Guide to ASAR Geocoding. Ref. RSL-ASAR-GC-AD, Issue 1.01*. RSL, University of Zürich. http://www.geo.uzh.ch/microsite/rsl-documents/research/publications/other-sci-communications/2008_RSL-ASAR-GC-AD-v101-0335607552/2008_RSL-ASAR-GC-AD-v101.pdf.

Trudel, M., Charbonneau, F., & Leconte, R. (2012). Using RADARSAT-2 polarimetric and ENVISAT-ASAR dual-polarization data for estimating soil moisture over agricultural fields. *Canadian Journal of Remote Sensing, 38*(4), 514–527. https://doi.org/10.5589/m12-043.

Wilford, J. R., Searle, R., Thomas, M., Pagendam, D., & Grundy, M. J. (2016). A regolith depth map of the Australian continent. *Geoderma, 266,* 1–13. https://doi.org/10.1016/j.geoderma.2015.11.033.

Worthington, S. R. H., Davies, G. J., & Alexander, E. C. (2016). Enhancement of bedrock permeability by weathering. *Earth-Science Reviews, 160,* 188–202. https://doi.org/10.1016/j.earscirev.2016.07.002.

Wright, E. P. (1992). The hydrogeology of crystalline basement aquifers in Africa. *Hydrogeology of Crystalline Basement Aquifers in Africa Geological Society Special Publication, 66,* 1–27. https://doi.org/10.1144/GSL.SP.1992.066.01.01.

Yu, B., Liu, G., Liu, Q., Wang, X., Feng, J., & Huang, C. (2018). Soil moisture variations at different topographic domains and land use types in the semi-arid Loess Plateau, China. *CATENA, 165,* 125–132. https://doi.org/10.1016/j.catena.2018.01.020.